Combustion and Flame 176 (2017) 220–228

Contents lists available at ScienceDirect

Combustion and Flame

journal homepage: www.elsevier.com/locate/combustflame

Nanoaluminum/Nitrocellulose microparticle additive for burn enhancement of liquid fuels

Philip M. Guerieri, Jeffery B. DeLisio, Michael R. Zachariah*

University of Maryland, College Park, MD 20740, United States

ARTICLE INFO

Article history:
Received 25 May 2016
Revised 18 October 2016
Accepted 19 October 2016

Keywords:
Nanoaluminum
Nitrocellulose
Electrospray
Fuel additives
Droplet combustion

ABSTRACT

Addition of metal and metal oxide nanoparticles to hydrocarbon fuels has shown the ability to increase the volumetric energy density, decrease ignition delay, increase heat of combustion, and catalyze fuel decomposition in recent research. However, energetic metal nanoparticles are prone to aggregation, which occurs at an increased rate near the regressing surface of a burning liquid droplet where local concentrations increase and can form a transport-inhibiting shell, ultimately decreasing the droplet burning rate. Alternatively, gas ejections from the droplet can disrupt shell formation and transport nanoparticles from the droplet to the flame zone. This study quantifies up to a 12.1% decrease in the burning rate constant of Kerosene droplets when 6.1 wt% nanoaluminum (nAl) particles are added (the maximum stable loading) with a hydrocarbon-based surfactant in a free-falling single droplet combustion experiment. Addition of nitrocellulose (NC) particles to the nanofuel diminishes or fully counteracts the burning rate decreases and provides a means of tuning the burning rate constant higher than that of pure Kerosene (maximum 13.8% increase over control with 2.3 wt% nAl and 0.6 wt% NC added). To reach stable nanofuels at higher particle loadings up to 15.0 wt% solid additives, nAl and NC were electrosprayed into composite mesoparticles (MP) before suspending with surfactant in Kerosene. These MP-based nanofuels boast increased dispersibility and additive loadings and thus higher achievable burning rates (maximum 26.5% increase over control) than physically mixed analogs. A mechanism is proposed in which droplet disruptions influenced by NC addition include cyclical inflations, during which the liquid gasification rate increases, e.g. by expanding the outer surface area of the droplet.

1. Introduction

Compared to their micron-sized counterparts, metal nanoparticles (NPs) generally boast shorter ignition delays and higher burning rates in combustion systems due to their increasing surface to volume ratio as particle size decreases [1]. In 1995, Choi and Eastman were the first to demonstrate that smaller particle size also enables the formulation of “nanofluids” in which repulsive electrostatic forces and Brownian motion counteract gravitational settling to suspend the NPs in the liquid [2]. Research has emerged over the last decade investigating the effects of various NP additives in liquid fuels, in particular “nanofuels”, which can feature increased energy densities, shortened ignition delay times, higher heats of combustion, decreased emissions, and promotion of evaporation and combustion rates. The high density-specific enthalpy of combustion of metals can be exploited to increase the volumetric energy density of a fuel or explosive upon NP addition [1,3,4]. A variety of NP additives have been shown to decrease NO_x, hydrocarbon, and/or CO emissions when added to diesel fuel for CI engines including Al [5–7], Al_2O_3 [6], Fe [7], B [7], CeO_2 [8], Fe_3O_4 [9], and Carbon Nanotubes (CNT) [10]. Research on nanofuels composed of jet fuels, monopropellants, or other hydrocarbons [11–26] has included metal oxide particles participating directly or catalytically in the oxidation of JP-10 in an atomized flow reactor [11], nanoaluminum (nAl) reducing the apparent ignition delay of JP-8 in a rapid compression machine [12], and increased burning rates of nitromethane in pressure vessels with the addition of functionalized graphene sheets [13], silica [14,15], AlOOH [13], Al_2O_3 [15], or nAl [14,16].

Droplet evaporation and combustion studies have identified important interacting processes and mechanisms active upon NP addition [17–26]. Radiative absorption of the additive from the flame, increased heat of combustion upon additive ignition, and droplet disruptions causing physical mixing and secondary atomization all promote evaporation and burning rates of nanofuel droplets [17–22]. Combusting slurries composed of micron-sized particles studied prior to 1990 suffered problematic effects due to particle agglomeration including low burning rates and combustion

* Corresponding author.
E-mail address: mrz@umd.edu (M.R. Zachariah).

http://dx.doi.org/10.1016/j.combustflame.2016.10.011
0010-2180/

efficiencies [27]. While transitioning from micron- to nano-particles significantly decreases the burning time and ignition delay of the solids, NPs are still particularly prone to agglomeration that frequently necessitates chemical stabilization which can inhibit particle combustion [1]. Even when a stable nanofuel is attained, the NP mass fraction increases near the surface of the droplet as liquid gasifies during combustion, thereby forming agglomerated shells and inhibiting transport [28]. NP agglomeration has been shown to occur at a timescale similar to that of droplet evaporation and burning, in many cases delaying the additive's participation in combustion (by induced gas generation or agglomerate ignition) to the late stages of the droplet lifetime and mitigating evaporation or burning rate increases [17,20,23] or even decreasing droplet evaporation rates [24,25].

Of these mechanisms, droplet disruption seems particularly capable of affecting burning rates by counteracting the formation of particle agglomerates, increasing physical mixing within the droplet (promoting species and thermal transport), deforming the droplet thereby changing the gas–liquid interfacial area, and causing secondary atomization of smaller droplets [28]. Disruptions are caused when the rate at which liquid is gasified within the droplet is higher than the rate at which the gas produced can escape, i.e. when internal gasification increases or multiphase transport decreases appreciably. Gasification rates can increase by a number of mechanisms including heterogeneous nucleation or localized heating around absorbing or reacting particles. When a droplet includes multiple liquid components with differing boiling points, one component can become superheated by the other and gasifies rapidly causing disruptions [29–32]. Particle agglomeration, especially when a shell is formed, will also induce disruptions by inhibiting transport of gasified products through the agglomerates until the gas pressure exceeds the inter-particle forces and the gas is rapidly released from the droplet [4,28]. Miglani and Basu have highlighted the apparent feedback loop between agglomerate shell formations and disruptions dismantling agglomerates or inhibiting shell growth [28]. The study found that dense particle loadings caused strong shell formation dominating over gas ejections which were largely suppressed, while dilute loadings showed high ejection frequencies that inhibited shell formation [28]. Since dominant agglomeration depresses the burning rate while disruptions enhance it, this interplay of mechanisms is a possible reason for the variety of burning rate effects observed in literature with NP addition. The dominating process can be dictated, and thus burning rate influenced, by modifying the additive to affect either droplet disruptions or particle agglomeration, namely by including a gas generating additive and/or modifying the particle morphology.

The current study investigates the effects of chemically stabilized nAl-based additives to Kerosene fuel with and without a gas-generating polymeric co-additive, Nitrocellulose (NC), in a drop-tower configuration designed to estimate combustion rates in the presence of disruptive burning [4]. Physical mixtures of the co-additives are compared with a composite mesoparticle additive of nAl electrosprayed in a NC matrix. Suspension stability is assessed and disruptive combustion is characterized by observing and measuring shadowgraphs of burning droplets suspended on a Silicon Carbide (SiC) monofilament.

2. Experimental

2.1. Nanofuel preparation

Nanoaluminum particles were used as-received from Novacentrix, Inc. (80% active Al with 2–5 nm oxide shell; Fig. 1(A)) for nAl nanofuel preparations and to assemble nAl–NC mesoparticles (MPs). The MPs, as well as NC particles for nAl–NC physical mixtures, were assembled by electrospray synthesis described by Wang et al [33]. The MP precursor consisted of 400 mg of nAl and NC solids (ranging from 5% to 20% NC) in 4 mL of 3:1 ethanol:diethyl ether while the NC precursor was mixed by dissolving 200 mg of NC solids (dried from collodion solutions of 4–8 wt% in ethanol/diethyl ether purchased from Fluka Corp.) in 2 mL of acetone. All precursors were agitated in a sonication bath for 1 h, and magnetically stirred for 24 h before electrospraying. Consistent with the electrospray procedure of Wang et al., precursors were fed at 4 mL/h through a 0.43 mm ID stainless steel probe needle by a syringe pump. The needle was charged to (+) 10 kV and aluminum foil substrate to (−) 10 kV at a distance of 10 cm from the probe needle. SEM of particles produced are shown in Fig. 1(B) and (C).

A surfactant was required to chemically stabilize the additive particles in the nanofuels. Trioctylphosphine oxide (TOPO), consisting of two long carbon chains (for compatibility with non-polar hydrocarbons) joined by a polar group (to combine with metal oxide on NP surfaces) was proposed for this purpose by E et al. to stabilize boron in JP-10 [34]. TOPO was added to all nanofuels in this study (2:1 TOPO:nAl by mass unless stated otherwise) and facilitated stable nAl suspensions up to 6.1 wt% and nAl/NC MP suspensions up to 15.0 wt%.

Nanofuels were assembled by adding specified solid loadings (either nAl, NC, nAl and NC, or nAl/NC MPs) to 0.5 mL of premixed TOPO in Kerosene (reagent grade from Sigma-Aldrich Co. LLC.) solutions. The same TOPO/Kerosene solutions were used as control fuels without additives for each loading. To promote suspension, nanofuel mixtures were agitated in a sonication bath for 1 h and magnetically stirred continuously until use (at least 24 h). 1 min of sonication also preceded all combustion experiments. MP nanofuels, which showed generally higher suspension stability than nAl or NC particle nanofuels and therefore required less agitation for

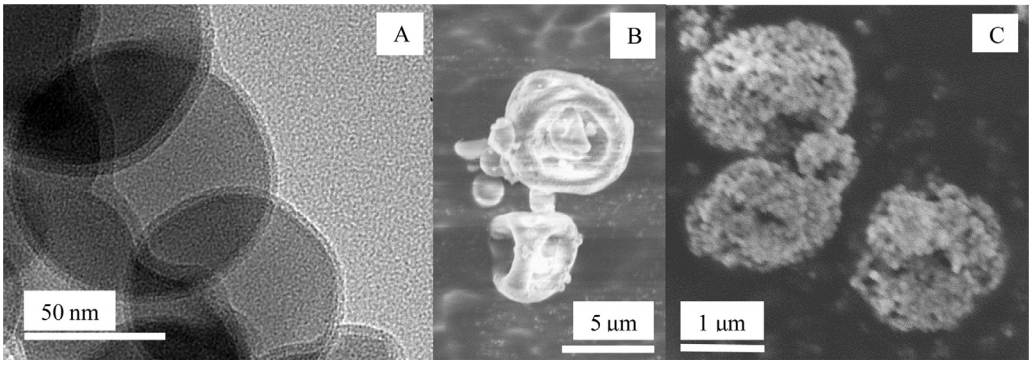

Fig. 1. (A) Nanoaluminum particulate additive TEM showing 2–5 nm oxide shell. (B) SEM of electrosprayed NC particles ranging from 1–6 μm in diameter. (C) nAl/20%NC mesoparticle SEM showing 1–2 μm diameter assemblies of ~80 nm nAl primary particles.

suspension, were only sonicated for 5 min before stirring to prevent MP damage.

2.2. Combustion characterization

Burning rate constants are evaluated using a drop tower configuration described in previous work[4] in which a ~0.6 mm diameter fuel droplet is generated and released to fall past two counterflow methane pilots and through 20 vertical inches of pure oxygen at room temperature. This recent method [4] avoids interference of any suspending filaments and the nonphysical assumption that the droplet volume indicates the mass of unburnt fuel remaining, which is otherwise required for classical burning rate measurements (using the slope of D^2 versus time). One high speed camera records a magnified shadowgraph (generated with an expanded HeNe laser and lens train) of the droplets passing the pilots to measure the initial droplet size (4–5 frames per droplet) while a second synchronized camera records the droplet flame falling through the tower. MATLAB image processing is used to measure the cross-sectional pixel area of droplets passing the igniters, calculate the equivalent circular diameter, and evaluate the eccentricity of the droplet. Calibrating for camera magnification with the known-diameter igniter tubes and eliminating frames of deformed droplets with eccentricity greater than 0.6 (where 0 is a circle and 1 in a line), each initial droplet diameter is calculated from the average of at least 3 admissible frames collected. The uncertainty of this average is estimated to be ±0.01 mm (an improvement upon method of [4] with higher camera magnification). MATLAB image processing also detects the first light and last light of each droplet flame falling through the tower to assess burning time with an estimated uncertainty of ±3 ms for the most faintly emitting samples (pure kerosene). The burning time and initial droplet diameter are used to estimate a burning rate constant by assuming all initial reactive material has burned upon flame extinction (i.e. $D_{Extinction}=0$) using Eq. (1) with a measurement uncertainty of ±0.02 mm^2/s. This assumption has been supported by TGA and XRD analyses of solid residues collected from falling droplets in previous work [4] and TGA of oxidized nAl residues from suspended droplet experiments discussed later. By averaging K estimates of approximately 8–12 droplets per trial, K is evaluated for each sample with an estimated experimental uncertainty of ±0.1 mm^2/s.

$$K = \frac{1 - D^2_{Extinction}/D^2_0}{t_{Extinction}/D^2_0} \cong \frac{{D_0}^2}{t_{Extinction}} \quad (1)$$

To further assess droplet disruptions during combustion, an alternative configuration employs a horizontal SiC monofilament (0.1 mm diameter; Goodfellow USA) to suspend a droplet in the center of the tower by pipetting a drop manually onto the filament. A methane pilot is then swept past the droplet for ignition and the same camera/laser shadowgraph setup described previously records a magnified image of the droplet combusting in place. The tower atmosphere used in suspended droplet experiments is air instead of oxygen to prevent the filament from igniting. MATLAB is used to measure the cross-sectional area of the droplet (with the filament subtracted) every two frames (334 µs), from which an equivalent spherical droplet diameter can be estimated. The initial droplet diameter is measured over at least 100 frames prior ignition and an ignition time is estimated using the inflection point of the initial increase in droplet diameter which occurs upon heating. The droplet diameter evolution over time can then be plotted to visualize the droplet disruptions over its entire combustion lifetime. While insight into the disruptive nature of each formulation is provided by this method to facilitate comparisons, quantitative burning rates are obscured by gas generation and solid combustion products within the droplets and are incomparable to the drop tower configuration due to the oxidizer change and conductive filament interference. Residue remaining on the filament after each sample burns is transferred to carbon tape on an SEM substrate for analysis and the filament is cleaned with Acetone before the next trial.

Table 1
Nanofuel suspension loading ranges.

Sample	wt% nAl	wt% NC	% Change in Energy Density	
			by volume	by mass
nAl NPs	2.3–6.0	N/A	1.1–3.3	−0.59 to −1.7
NC NPs	N/A	0.13–1.3	0.06–1.0	−0.10 to −1.8
nAl + NC NP Phys Mix	2.3–6.0	0.13–0.70	1.1–3.0	−0.69 to −2.2
nAl/5%NC MPs	2.3–12.4	0.13–0.65	1.1–8.1	−0.69 to −4.6
nAl/10%NC MPs	2.3–12.4	0.23–1.4	1.0–7.6	−0.79 to −5.3
nAl/15%NC MPs	2.3–12.4	0.40–2.1	0.94–7.0	−0.90 to −6.0
nAl/20%NC MPs	2.3–12.4	0.57–3.0	0.86–6.4	−1.0 to −6.9

3. Results and discussion

3.1. Suspension stability

Particle loading ranges for all samples were maximized based on their propensity to pump through the droplet generation capillary reliably. nAl particle suspensions clogged the delivery needle at loadings > 6.1 wt% and NC suspensions at > 2.3 wt%. MPs suspensions however can be mixed up to 15.0 wt% particles for MPs composed of 80 wt% nAl and 20 wt% NC ("nAl/20%NC MPs") before clogging begins. In order to electrospray particles instead of fibers, the binder content of the MP composite is limited to 20% or less NC polymer and thus four MP types were used (nAl/5wt%NC, nAl/10wt%NC, nAl/15wt%NC, and nAl/20wt%NC). nAl+NC physical mixture suspensions were chosen to match the constituent loadings of the MP samples up to 6.0 wt% nAl NPs +0.7 wt% NC particles ("6.7wt% nAl + 10%NC PM"), with higher loadings causing clogs. Based on these limits, Table 1 summarizes the samples formulated and tested and the theoretical change in volume and mass-based energy densities (enthalpies of combustion with oxygen per volume or mass) the additives would cause in dodecane without TOPO surfactant considered.

Long term stability of the nanofuels was assessed qualitatively by allowing the suspensions to gravitationally settle for 1 week following combustion testing and visualizing the suspension quality. Representative suspensions of 6.1 wt% nAl, nAl/5%NC MPs, and nAl/20%NC MPs were also sonicated and stirred in kerosene without surfactant before pouring into clean vials and allowing to gravitationally settle for 1 day to illustrate dispersibility without chemical stabilization. With TOPO, all physical mixture nanofuels settled out of suspension within 1 week while MP samples maintained suspension (photographs available in Supplemental Information). Without surfactant, nAl failed to suspend at 6.1 wt% with most of the nAl and kerosene gelling during the magnetic stirring and adhering to the mixing vial. The MP samples do suspend but gravitationally settle more without surfactant after 1 day. The presence of NC polymer in the MPs with the nAl is the likely cause of increased dispersibility of MPs relative to nAl with and without TOPO. NC has polar and nonpolar sections but overall has a lower dielectric constant (~6.2–7.5) than the alumina surfaces of nAl (~9.3–11.5). Since kerosene has a low dielectric constant (~1.8–2.8), the NC will disperse better than alumina in kerosene. MPs have more alumina surfaces covered in NC than do nAl particles (with or without NC particles added) and therefore will disperse better than nAl. Adding TOPO surfactant will increase the stability of both nAl physical mixtures and MPs since it has a polar end which is compatible with any exposed Alumina and hydrocarbon chains compatible with the kerosene.

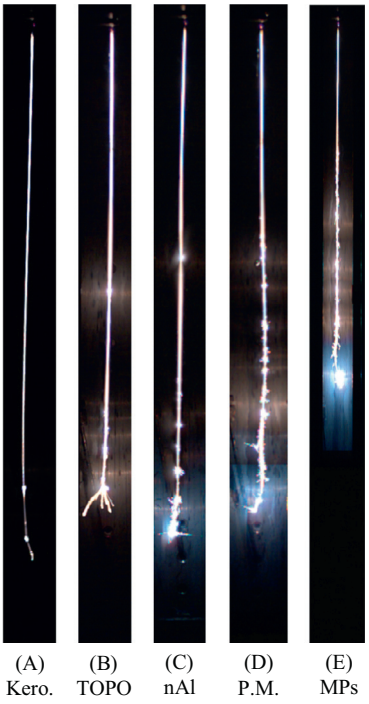

Fig. 2. Time-lapse images of falling, combusting Kerosene droplets with 120 mg/mL TOPO surfactant, unless noted otherwise, and various nanoparticle additives. (A) Kerosene only (no TOPO). (B) 120 mg/mL TOPO control. (C) 6.1 wt% nAl. (D) 6.7 wt% nAl+ 10%NC physical mixture. (E) 6.7 wt% nAl/10%NC mesoparticles.

3.2. Nanofuel falling droplet combustion

Figure 2 depicts time-lapse images of five representative samples combusting in the falling droplet experiment. When applicable, the samples shown include the same mass loading of TOPO surfactant (B-E), nAl (C-E), and NC (D-E). Disturbances in the trace of visible flame radiation are attributed to droplet disruptions during which gas is ejected from the droplet, on occasion carrying condensed phase reactants or causing a fission event, and usually preceded by droplet inflation. Suspended droplet experiments discussed later provide detailed evidence for and analysis of these disruptions. The falling motion of the droplets, deviations of their trajectories from the centerline, and apparent stochastic disruption events render magnified videography and classical D^2 burning rate analysis on the falling droplets unviable.

Any nAl added combusts predominantly in the final stage of combustion, when little to no liquid fuel remains (indicated by obvious color temperature increase in Fig. 2(C)–(E) characteristic of Al combustion). While slurry fuels behave similarly [27], their slow-burning micron-particles comprise a significantly larger fraction of the overall burning time compared to the rapid combustion of nAl in liquid fuels. When disruptions liberate secondary small droplets, minute amounts of nAl can also combust near their termination, before the final stages of the parent droplet combustion. Presumably nAl could escape unburned from a system without ample energy to ignite the solids; however, TGA data confirms that residues collected from suspended droplet experiments contain little to no reactive aluminum suggesting near-complete nAl combustion here in kerosene–air. Flame temperatures of the kerosene–oxygen system in falling droplet trials are even higher than those of kerosene–air which together with evident emission characteristic of nAl in the color videos suggests thorough combustion of nAl in the fuels.

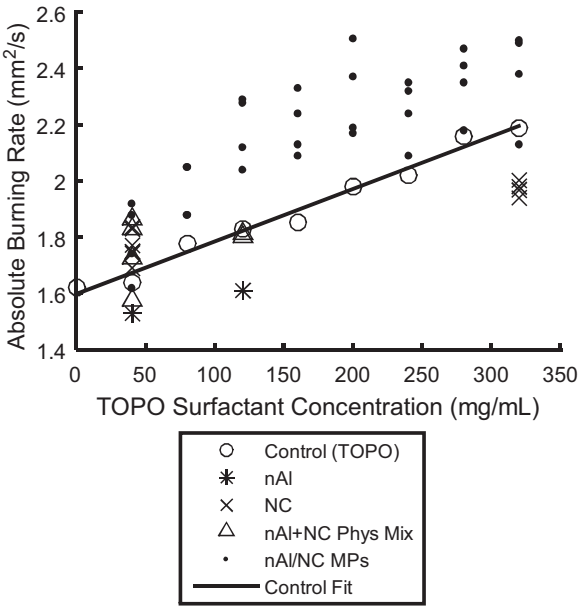

Fig. 3. Absolute burning rate constants versus control surfactant concentration.

3.3. Burning rate measurements

Because the TOPO surfactant concentrations vary among the samples tested with the nAl additive concentration, the surfactant effect on the burning rates must be assessed so additive effects can be normalized with respect to TOPO control data. Addition of the surfactant increases the burning rate linearly with an *R*-squared fit value of 0.955 (plot of absolute burning rates versus surfactant concentration with TOPO control trendline shown in Fig. 3). Time-lapse images of falling droplet trials show increased visible flame radiation and onset of a characteristic late explosion which can disperse small secondary droplets with increasing TOPO concentrations. All subsequent burning rates are represented as percent change relative to the burning rate of the corresponding TOPO solution measured on the same day to eliminate environmental variations. Considering the estimated experimental uncertainty of the burning rate constant, the maximum uncertainty of the percent change in burning rate is estimated to be ±8%.

Nitrocellulose addition is of interest due to its preexisting role as a composite particle binder and its expected role as a gas generating additive to incite droplet disruptions for burning rate enhancement. To investigate its influence without nAl present, NC is assembled into microparticles and added to kerosene fuels with two TOPO concentrations (the minimum and maximum surfactant loadings used in the study). Flame trace observations depict little to no significant qualitative effects of added NC on visible flame radiation or apparent droplet disruptions relative to respective TOPO solution controls (representative time-lapse images available in Supplemental Information). Resultant burning rate effects are plotted in Fig. 4 as functions of NC particle loading. At low surfactant concentration, NC addition causes burning rate enhancement up to a critical loading (12.9% increase at 0.5 wt% NC) beyond which the enhancement decreases. However, at high surfactant loadings, the NC enhancement is masked by the burning rate increase of the TOPO. 320 mg/mL TOPO causes a 33.5% increase in burning rate relative to 40 mg/mL TOPO. If the mechanisms of the NC and TOPO additions without nAl were mutually exclusive, thereby counteracting each other, a decrease much greater than the observed 5% would be expected with NC addition to 320 mg/mL TOPO. This shows that instead, the mechanisms of NC and TOPO added without nAl to kerosene are likely

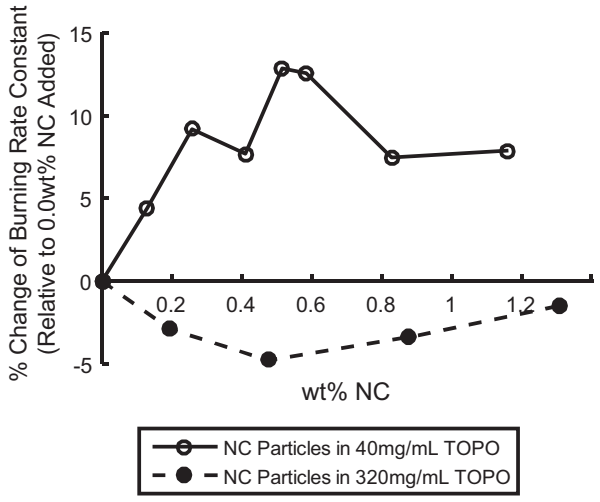

Fig. 4. Effect of nitrocellulose particles on droplet burning rates.

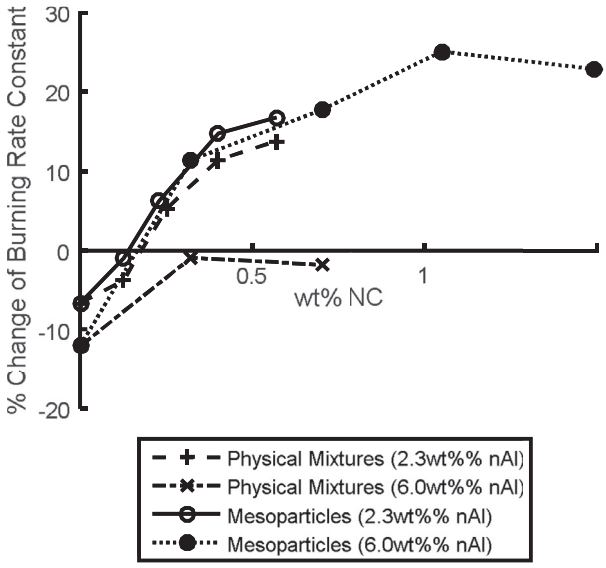

Fig. 5. Burning rate effects of nAl/NC physical mixture and mesoparticle additives. Y-intercepts are nAl particle suspensions in all cases. Burning rate % changes are relative to the TOPO surfactant-only control solution for each data point (2:1 TOPO:nAl by mass).

similar, such that relatively small NC addition to an already highly TOPO-laden sample simply incites no further enhancement. Despite this, NC added to kerosene can clearly increase the burning rate and even provide means of tuning with NC concentration.

nAl was added to the fuel in two forms: as-received NPs and within mesoparticle composite assemblies with NC. The effects of these configurations can be directly compared up to the maximum loading of nAl NPs (6.1 wt%). To do so, physical mixtures of nAl + NC particles and MPs of equal constituent loadings were formulated and their burning rate effects are plotted in Fig. 5 as functions of each nanofuel's NC concentration. The two *y*-intercepts denote as-received nAl without NC added in all cases (since MPs cannot be assembled without a polymeric binder). While nAl addition alone decreases the burning rate with increasing concentration, this decrease can be counteracted by adding NC to increase the burning rate. The net effect is a nanofuel that burns with the same or higher burning rate as the control with the added theoretical energy density of the nAl component. At low loadings (2.3 wt% nAl), the physical mixture and MPs behave the same showing no

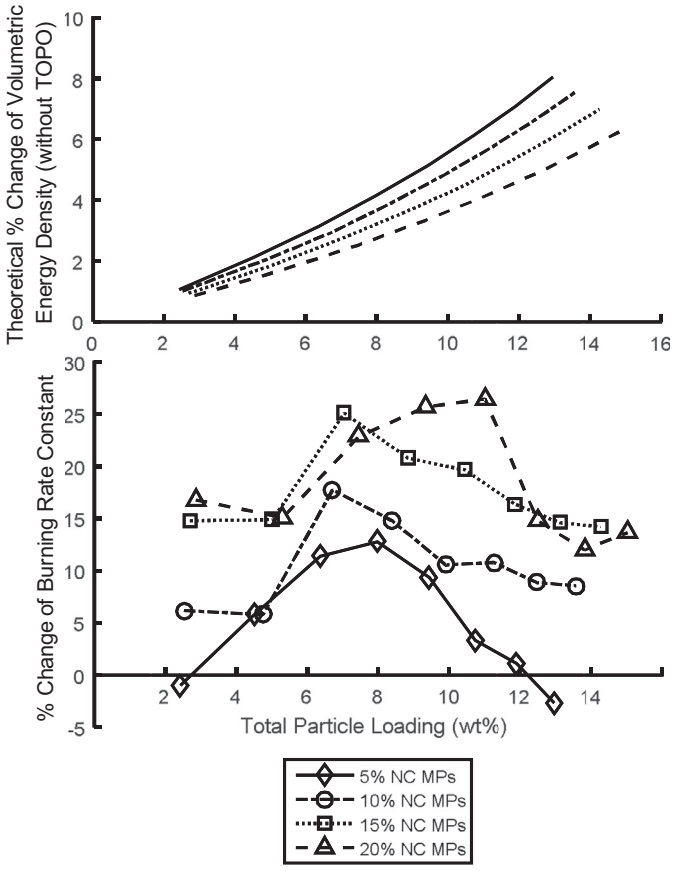

Fig. 6. (Top) Theoretical increase in volumetric energy density of kerosene fuel as functions of composite mesoparticle additive loading based on enthalpy of combustion with oxygen per volume of nanofuel. (Bottom) Effect of composite mesoparticle loadings on droplet burning rates. Burning rate % changes are relative to the TOPO surfactant-only control solution for each data point (2:1 TOPO:nAl by mass).

benefit of one architecture over the other. At higher loadings however, the MPs follow the same trend as low loadings while the burning rate of the physical mixtures are depressed by the increased nAl addition. The MP architecture with 6 wt% nAl also facilitates higher stable NC loadings (>0.7 wt%). In the analogous 6 wt% nAl physical mixtures, NC loadings > 0.7 wt% cause sample agglomeration and needle clogging. Consistent with its effect without nAl, NC provides a means of tuning the burning rate and compensating for decreases caused by nAl addition. Assembly into MPs expands the range of tuning available.

Recalling that assembling the NC and nAl into MPs maintains suspension stability at higher loadings than physical mixtures, the burning rate enhancement of such higher loadings are shown in Fig. 6 plotted versus total particle loading and organized by the nAl:NC ratio (i.e. MP type). Note that in all cases, the absolute burning rates increase with particle loading when the TOPO effect is considered. When normalizing by this effect, it is evident that (similar to NC particle addition) MPs cause burning rate increases up to critical loadings beyond which the burning rate enhancements diminish. Higher NC content in most cases also increases the enhancement as expected; however, 15% and 20% NC burning rates are similar indicating minimal marginal benefit of increasing the NC content beyond 15%. In all but two data points, addition of nAl/NC MPs increased the burning rate to some extent and since they can be used to reach higher loadings, a greater maximum burning rate enhancement over controls is also observed compared to physical mixtures (MP maximum 26.5% burning rate increase; physical mixtures maximum 13.8% burning rate increase). NC

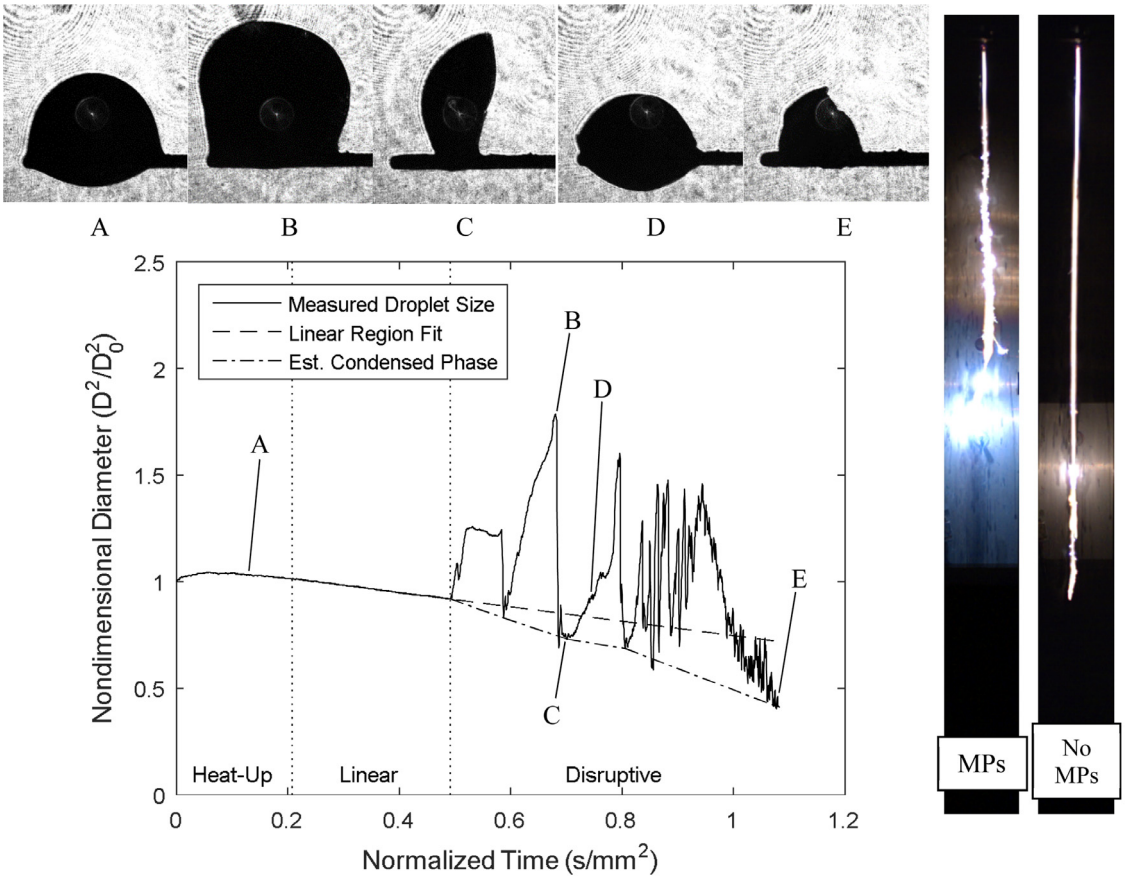

Fig. 7. 10.4 wt% nAl/15%NC MPs in 200 mg/mL TOPO/Kerosene. (Left) Representative annotated data of suspended droplet size evolution during combustion on a SiC filament in air. (Right) Time-lapse images of 200 mg/mL TOPO/Kerosene with and without MPs added. Plots for all thirteen samples tested as suspended droplets with representative falling droplet time-lapse images available in Supplemental Information.

addition decreases the net volumetric energy density of the fuel, an effect opposite to that observed with nAl addition. Fig. 6 quantifies this effect theoretically over the range of MP loadings studied based on calculating the change in enthalpy of combustion per unit volume that results from adding the corresponding quantities of Al and NC to dodecane. Added NC content can increase the burn rate of the composite particles while the nAl content increases the theoretical enthalpy of combustion per volume relative to the liquid fuel; however, since NC has a lower volumetric energy density than that of kerosene, this increase in burn rate incurs a penalty in the resultant energy density increase as illustrated in Fig. 6. Both MP additive loading and NC percentage in the MPs provide a fuel designer with means of tuning the burning rate and energy density increases of the composite fuel.

3.3.3. Droplet disruption analysis

Direct observation of burning clearly shows that a classical D^2-type analysis is not applicable since significant fission events during burning are observed. Figure 7 depicts a representative plot of droplet size evolution during its burning on a horizontal SiC filament in air with time-lapse images of falling droplets with and without MP additive (plots and time-lapse images for all thirteen representative samples tested as suspended droplets are available in the supplemental information). The filament is not completely insulating (with slight preferential boiling observed near the droplet–filament interface) and air is required rather than oxygen to prevent combustion of the filament. Gas generated during disruptions and solid products in the droplets also obscure any burning rate measurements by decoupling the cross-sectional area observed from the mass of unreacted fuel remaining [28,35]. As such, the stationary experiments are not quantitatively equivalent to the falling droplet experiments but facilitate comparison of the disruptions caused by various additives. Supplemental Information includes suspended droplet data next to falling droplet time-lapse images for various samples illustrating that qualitatively, the disruptive natures of the fuels are approximately preserved between the two experiments and thus the suspended droplet experiments can provide insight into disruption effects.

Three distinct combustion regimes are evident in the stationary droplet evolution plots: an initial non-linear heat up region during which flame energy heats the droplet to its boiling point (expanding it); a subsequent linear combustion region akin to classical droplet combustion; and ultimate disruptive regions characterized by deviations from classical (linear) droplet burning by repeated inflations, deflations, and shape perturbations from momentum transfer upon gas or condensed phase ejections. We find that shorter times (normalized by square of initial droplet diameter) to the first of these disruptive regions in suspended droplet experiments roughly correlate ($R^2 = 0.829$) with faster burning rates measured in falling droplet experiments (plotted in Supplemental Information). The surface area increase due to inflation can be estimated from this data during the disruptive regimes. Disruptive regions are subdivided by local minimums which roughly represent the droplet with little to no internal gas. The approximate volume of condensed phases in the droplet can therefore be interpolated between these two points for each sub-region (shown as dash-dot lines in Fig. 7) and by comparison with the actual volume measured, the difference provides an estimate of droplet

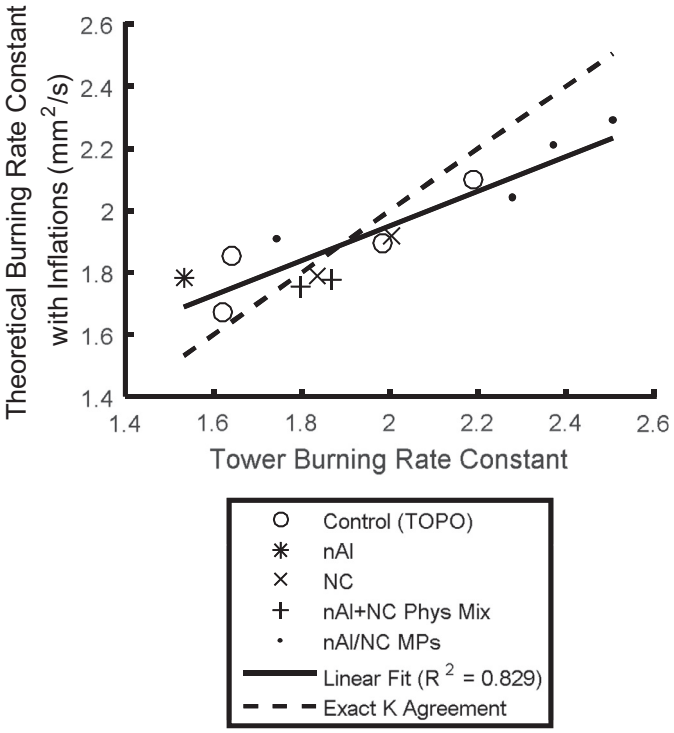

Fig. 8. Theoretical burning rate constants based on enhancement of surface gasification caused by droplet inflations in suspended droplet experiments versus burning rate constants measured in falling droplet experiments.

inflation volume that results from internal gases. Assuming constant values of vapor diffusion coefficients, vapor mass fractions at the droplet, and vapor mass fractions in the ambient environment, the rate of phase change per surface area at the droplet is inversely proportional to the droplet diameter. By fitting the proportionality constant to data obtained for pure kerosene which is devoid of any disruptions ($\alpha = 0.963$), the added volume gasified due to increases in droplet surface area by inflations over the droplet lifetime is estimated and normalized by initial droplet volumes (expressed as volume percent) and residue volumes (final solid product volumes measured are assumed to form within the droplet linearly over their lifetimes and are subtracted) and given by Eq. (2), plotted in Supplemental Information.

$$\left(\frac{V}{V_0}\right)_{\text{Inflation}} = \alpha \int_0^{\frac{t}{D_0^2}} \left(\frac{D_{\text{Inflated}}}{D_0}\right) - \left(\frac{D_{\text{Deflated}}}{D_0}\right) dt \tag{2}$$

By assuming that a hypothetical droplet burning in the tower without this enhancement will do so at the rate observed for pure kerosene droplets in falling droplet experiments ($\bar{K}_{\text{Kerosene}} = 1.62$), the effect of this added volume loss by increased surface gasification from inflations on the burning rate constant can be estimated theoretically by Eq. (3) and compared with the actual burning rate constants observed in Fig. 8.

$$K_{\text{Inflation}} = \frac{\bar{K}_{\text{Kerosene}}}{1 - \left(\frac{V}{V_0}\right)^{1.5}_{\text{Inflation}}} \tag{3}$$

The linear correlation observed suggests that inflation is a strong mechanism by which these disruptive samples affect overall burning rates. The theoretical burning rate constants that would result from this effect are similar to the actual burning rate constants observed, proving that the magnitude of this mechanism can be large enough to account for much of the enhancements observed. However, since the proportionality constant is less than one (exact agreement), inflations also likely enhance the burning rate by mechanisms other than outer droplet surface area increase.

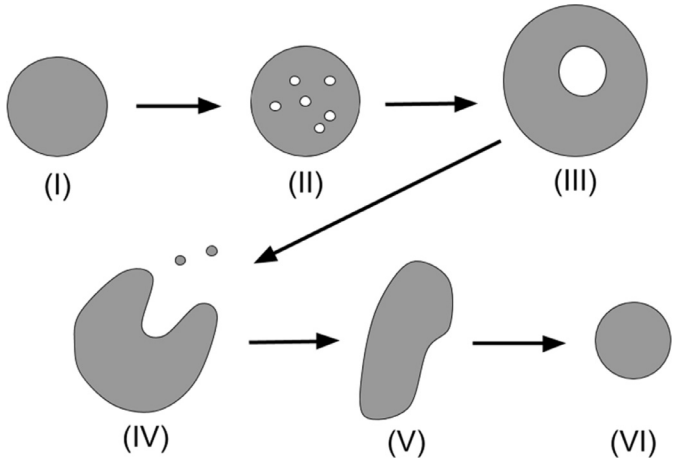

Fig. 9. Schematic of cyclical droplet inflation and deflation. Increased surface area during inflations promote gasification at outer surfaces and promotes burning rate. (I) Undisturbed droplet. (II) Gas bubbles nucleate by radiative heat absorption gasifying local fluid, thermal decomposition of NC, and/or multicomponent superheating [29–33]. (III) Gas bubble coalescence. (IV) Ejection. (V) Momentum transfer and shape deformation. (VI) Droplet equilibration and repeat.

3.4. Proposed additive mechanisms

Based on evidence from the suspended droplet experiments, droplet inflations are thought to be directly related to burning rate increasing mechanisms of disruptively burning droplets. A schematic of an inflation-deflation event is shown in Fig. 9. Inflations increase the outer surface area thereby promoting the gasification rate (II–V), facilitate internal gasification at newly formed liquid–gas interfaces (II–III), and can eject material upon deflation (IV).

The propensity of a droplet to inflate is affected by internal gas generation and effective surface tension. The equilibrium inflation volume is that which balances inward atmospheric pressure and Laplace pressure with outward gas pressure. This outward pressure is a function of the gas' mass, temperature, and volume. For constant internal gas mass and temperature, its volume will increase with decreasing Laplace pressure given in Eq. (4), where γ is surface tension, R_b is the radius of the internal bubble, and R_d is the radius of the droplet. Therefore, as surface tension decreases, inflations would be expected to increase for the same amount of internal gas generated. As the mass of gas liberated within the droplet increases, inflations also increase since the equilibrium inflation size (R_b and R_d) that balances the inward and outward forces on the condensed phase becomes larger.

$$\Delta P_{\text{Laplace}} = \gamma\left(\frac{1}{R_b} + \frac{1}{R_d}\right) \tag{4}$$

The soluble TOPO surfactant can both decrease the surface tension of the kerosene and increase gas generation since multicomponent combustion droplets with differing boiling points are known to generate gas internally [29–32]. This is consistent with the observed increase in both droplet inflations and burning rate with increasing TOPO concentration. Agreeing with multiple examples of increasing burning rates with increasing NC content, NC addition will also increase gas generation and consequential inflations since it is known to thermally decompose beginning at ~195 C which is lower than the boiling point of kerosene (the temperature that the droplet can be expected to reach and maintain in the ignition stage of its combustion). nAl can also promote inflations since it is known to increase radiative heat transfer from the flame to the droplet which can accelerate internal gasification and thermal decomposition processes [6,17,18,22]. Therefore, all

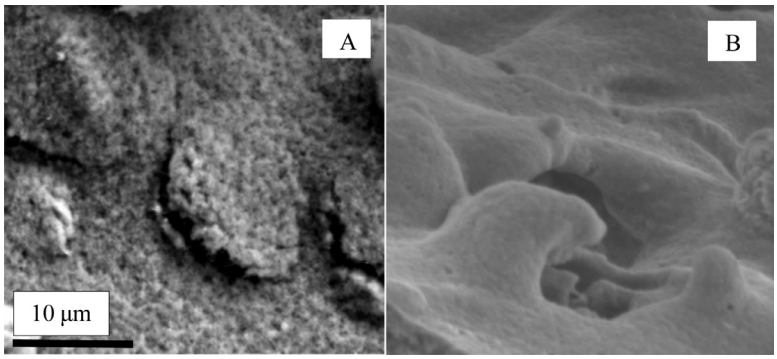

Fig. 10. SEM (1.8kX) depicting inner surfaces of residues of (A) 10.4wt% nAl/15%NC MPs in 200 mg/mL TOPO and (B) 2.9wt% nAl + 20%NC physical mixture in 40 mg/mL TOPO suggesting higher porosity of MP agglomerates relative to physical mixture agglomerates.

additives studied herein have mechanisms by which droplet inflations (and burning rates) can increase with increasing additive concentration.

However, inclusion of solid particles also adds the effects of particle transport and agglomeration to the inflation dynamics. As particle-laden droplets burn and the particle mass fraction increases, particle agglomeration increases, especially near the receding droplet surface resulting in shell formation. The characteristic time for a particle to diffuse the radius of the droplet is $\tau_{\text{Diff}} \approx \frac{(0.3\text{mm})^2}{D}$ where by the Stokes–Einstein equation, $D = \frac{k_B T}{3\pi \mu d_p}$. Assuming the viscosity of the droplet is approximately that of dodecane ($\mu = 1.34$ mPa-s), MP diameters are 1 μm, and NP diameters are 80 nm, the characteristic times are $\tau_{\text{Diff, MP}} \approx 1.6 \times 10^5$s and $\tau_{\text{Diff, NP}} \approx 1.3 \times 10^6$s which are much longer than the characteristic time of surface regression (equal to the burning time which is approximately 250 ms). Therefore, the surface will regress during combustion much faster than particles can diffuse inward, thereby forming a shell. Agglomerate shells will inhibit liquid and gas transport and therefore add an inward component to the force balance on a growing internal gas bubble. Similar to the effect of weak versus strong surface tension, an agglomerate held together with weak minimum interparticle forces will change shape and size and permit multiphase transport more easily (and thus induce less inward pressure on a growing bubble) than an agglomerate shell with strong minimum interparticle forces. Considering an agglomerate forming of nAl NPs (e.g. Fig. 1(A)) versus one forming of MPs (e.g. Fig. 1(C)), the top-level assembly particles are an order of magnitude different in size (nAl agglomerates are assembled of ~80 nm nAl NPs; MP agglomerates are composed of ~1 μm mesoparticle sub-assemblies). Thus, the overall strength of MP agglomerates is limited by the smaller contact areas and larger interparticle distances between individual MPs, a level of interparticle weakness which does not limit the strength of an nAl agglomerate. Figure 10 shows SEM of the inner surfaces of agglomerate residues recovered from suspended droplet experiments of nAl/NC MP (A) and nAl+NC physical mixture (B) nanofuels, respectively. The porosity of the MP nanofuel residue is noticeably higher than that of the physical mixture nanofuel, providing further evidence of smaller contact areas and larger interparticle distances in MP agglomerates. Therefore, MPs are expected to facilitate increased inflations relative to physically mixed analogs which are consistent with experimental observations. Particle agglomeration inhibiting droplet inflation can also explain decreases in burning rates observed at high particle loadings and in samples of nAl without NC.

4. Conclusions

Nitrocellulose is shown to be a suitable gas generator capable of increasing the burning rates of hydrocarbon droplets laden with nAl particles, which without this gas-generating co-additive would otherwise decrease the burning rate of the fuel. Physical mixtures of NC and nAl particles in kerosene are limited by poor stability with increasing particle loading, even with the use of TOPO, a hydrocarbon surfactant. However we find that composite nAl/NC mesoparticles can be used to create stable nanofuels with over twice the maximum particle loadings of physically mixed nanofuels without clogging the droplet generation capillary (analogous to propellant/fuel handling infrastructure). The MP additives also promote higher burning rates at increased loadings where detrimental agglomeration effects are more severe for physically mixed additives relative to MP additives. Cyclical droplet inflations and deflations are found to be an important mechanism whereby increased gasification rates, e.g. by enlarged droplet surface area exposed to the flame, promote the overall burning rate of the fuel which can be promoted by lowering fluid surface tension, increasing internal gas generation with absorbing particles or thermally decomposing additives, or by weakening particle agglomerates that form using the MP composite architecture.

Acknowledgments

This work was made possible from the support of an Air Force Office of Scientific Research MURI grant and the Defense Threat Reduction Agency. SEM and TEM performed in the UMD AIMLab. Special thanks to Professor Richard Yetter of Penn State University for providing the original droplet combustion tower apparatus.

Supplementary materials

Supplementary material associated with this article can be found, in the online version, at doi:10.1016/j.combustflame.2016.10.011.

References

[1] R. Yetter, G. Risha, S. Son, Metal particle combustion and nanotechnology, Proc. Combust. Inst. 32 (2009) 1819–1838.
[2] S. Choi, J. Eastman, Enhancing Thermal Conductivity of Fluids with Nanoparticles, ASME International Mechanical Engineering Congress & Exposition, San Francisco, CA (1995).
[3] E. Dreizin, Metal-based reactive nanomaterials, Prog. Energy Combust. Sci. 35 (2009) 141–167.
[4] P.M. Guerieri, S. DeCarlo, B. Eichhorn, T. Connell, R.A. Yetter, X. Tang, Z. Hicks, K.H. Bowen, M.R. Zachariah, Molecular aluminum additive for burn enhancement of hydrocarbon fuels, J. Phys. Chem. A 119 (2015) 11084–11093.
[5] M. Kao, C. Ting, B. Lin, T. Tsung, Aqueous aluminum nanofluid combustion in diesel fuel, J. Test. Eval. 36 (2008) 186–190.
[6] H. Tyagi, P.E. Phelan, R. Prasher, R. Peck, T. Lee, J.R. Pacheco, P. Arentzen, Increased hot-plate ignition probability for nanoparticle-laden diesel fuel, Nano Lett. 8 (2008) 1410–1416.
[7] R. Mehta, M. Chakraborty, P. Parikh, Nanofuels: combustion, engine performance and emissions, Fuel 120 (2014) 91–97.

[8] V. Sajith, C. Sobhan, G. Peterson, Experimental investigations on the effects of cerium oxide nanoparticle fuel additives on biodiesel, Adv. Mech. Eng. 2010 (2010), Article No. 581407.
[9] N. Sarvestany, A. Farzad, E. Ebrahimnia-Bajestan, M. Mir, Effects of magnetic nanofluid fuel combustion on the performance and emission characteristics, J. Dispers. Sci. Technol. 35 (2014) 1745–1750.
[10] N. Singh, R. Bharj, Effect of CNT-emulsified fuel on performance emission and combustion characteristics of four stroke diesel engine, Int. J. Curr. Eng. Technol. 5 (2015) 477–485.
[11] B. Van Devener, S. Anderson, Breakdown and combustion of JP-10 fuel catalyzed by nanoparticulate CeO_2 and Fe_2O_3, Energy Fuels 20 (2006) 1886–1894.
[12] C. Allen, G. Mittal, C. Sung, E. Toulson, T. Lee, An aerosol rapid compression machine for studying energetic-nanoparticle-enhanced combustion of liquid fuels, Proc. Combust. Inst. 33 (2011) 3367–3374.
[13] J. Sabourin, D. Dabbs, R. Yetter, F. Dryer, I. Aksay, Functionalized graphene sheet colloids for enhanced fuel/propellant combustion, ACS Nano 3 (2009) 3945–3954.
[14] J. Sabourin, R. Yetter, B. Asay, J. Lloyd, V. Sanders, G. Risha, S. Son, Effect of nano-aluminum and fumed silica particles on deflagration and detonation of nitromethane, Propellants Explos. Pyrotech. 34 (2009) 385–393.
[15] J. Sabourin, R. Yetter, V. Parimi, Exploring the effects of nanostructured particles on liquid nitromethane combustion, J. Propuls. Power 26 (2010) 1006–1015.
[16] K. McCown, E. Petersen, Effects of nano-scale additives on the linear burning rate of nitromethane, Combust. Flame 161 (2014) 1935–1943.
[17] Y. Gan, L. Qiao, Radiation-enhanced evaporation of ethanol fuel containing suspended metal nanoparticles, Int. J. Heat Mass Transf. 55 (2012) 5777–5782.
[18] Y. Gan, L. Qiao, Optical properties and radiation-enhanced evaporation of nanofluid fuels containing carbon-based nanostructures, Energy Fuels 26 (2012) 4224–4230.
[19] I. Javed, S. Baek, K. Waheed, G. Ali, S. Cho, Evaporation characteristics of kerosene droplets with dilute concentrations of ligand-protected aluminum nanoparticles at elevated temperatures, Combust. Flame 160 (2013) 2955–2963.
[20] I. Javed, S.W. Baek, K. Waheed, Effects of dense concentrations of aluminum nanoparticles on the evaporation behavior of kerosene droplet at elevated temperatures: The phenomenon of microexplosion, Exp. Therm. Fluid Sci. 56 (2014) 33–44.
[21] I. Javed, S. Baek, K. Waheed, Autoignition and combustion characteristics of heptane droplets with the addition of aluminium nanoparticles at elevated temperatures, Combust. Flame 162 (2015) 191–206.
[22] S. Tanvir, L. Qiao, Effect of addition of energetic nanoparticles on droplet-burning rate of liquid fuels, J. Propuls. Power 31 (2015) 408–415.
[23] Y. Gan, Y. Lim, L. Qiao, Combustion of nanofluid fuels with the addition of boron and iron particles at dilute and dense concentrations, Combust. Flame 159 (2012) 1732–1740.
[24] Y. Gan, L. Qiao, Evaporation characteristics of fuel droplets with the addition of nanoparticles under natural and forced convections, Int. J. Heat Mass Transf. 54 (2011) 4913–4922.
[25] I. Javed, S. Baek, K. Waheed, Evaporation characteristics of heptane droplets with the addition of aluminum nanoparticles at elevated temperatures, Combust. Flame 160 (2013) 170–183.
[26] Y. Gan, L. Qiao, Combustion characteristics of fuel droplets with addition of nano and micron-sized aluminum particles, Combust. Flame 158 (2011) 354–368.
[27] P. Choudhury, Slurry fuels, Prog. Energy Combust. Sci. 18 (1992) 409–427.
[28] A. Miglani, S. Basu, Coupled mechanisms of precipitation and atomization in burning nanofluid fuel droplets, Sci. Rep. 5 (2015) 15008.
[29] C. Law, Internal boiling and superheating in vaporizing multicomponent droplets, AIChE J. 24 (1978) 626–632.
[30] C. Law, Recent advances in droplet vaporization and combustion, Prog. Energy Combust. Sci. 8 (1982) 171–201.
[31] C. Wang, X. Liu, C. Law, Combustion and microexplosion of freely falling multicomponent droplets, Combust. Flame 56 (1984) 175–197.
[32] A. MAKINO, C. LAW, On the controlling parameter in the gasification behavior of multicomponent droplets, Combust. Flame 73 (1988) 331–336.
[33] H. Wang, G. Jian, G. Egan, M. Zachariah, Assembly and reactive properties of Al/CuO based nanothermite microparticles, Combust. Flame 161 (2014) 2203–2208.
[34] X. E, X. Zhi, Y. Zhang, C. Li, J. Zou, X. Zhang, L. Wang, Jet fuel containing ligand-protecting energetic nanoparticles: a case study of boron in JP-10, Chem. Eng. Sci. 129 (2015) 9–13.
[35] S. Basu, A. Miglani, Combustion and heat transfer characteristics of nanofluid fuel droplets: a short review, Int. J. Heat Mass Transf. 96 (2016) 482–503.